2006

Failure mechanisms in superplastic AA5083 materials

Kulas, Mary-Anne; Green, W. Paul; Taleff, Eric M.; Krajewski, Paul E.; McNelley, Terry R.

M.-A. Kulas, W.P. Green, E.M. Taleff, P.E. Krajewski, T.R. McNelley, "Failure mechanisms in superplastic AA5083 materials," Metallurgical and Materials Transactions A, v.37A, (March 2006), pp. 646- 655.
http://hdl.handle.net/10945/55844

Failure Mechanisms in Superplastic AA5083 Materials

MARY-ANNE KULAS, W. PAUL GREEN, ERIC M. TALEFF, PAUL E. KRAJEWSKI, and TERRY R. McNELLEY

The mechanisms of tensile failure in four 5083 aluminum sheet materials are evaluated under conditions of interest for superplastic and quick-plastic forming. Two mechanisms are shown to control failure of the AA5083 materials under uniaxial tension at elevated temperatures: cavitation and flow localization (*i.e.*, necking). Conditions for which failure is controlled by cavitation correspond to those under which deformation is primarily by grain-boundary-sliding creep. Conditions for which failure is controlled by flow localization correspond to those under which deformation is primarily by solute-drag creep. A geometric parameter, Q, is used to determine whether final failure is controlled by cavitation or by flow localization. Differences in elongations to failure between the different AA5083 materials at high temperatures and slow strain rates are the result of differences in cavitation behaviors. The rate of cavitation growth with strain is nearly constant between the AA5083 materials for identical testing conditions, but materials with less tensile ductility evidence initial cavitation development at lower strain levels. The rate of cavitation growth with strain is shown to depend on the governing deformation mechanism; grain-boundary-sliding creep produces a faster cavitation growth rate than does solute-drag creep. A correlation is found between the early development of cavitation and the intermetallic particle-size population densities of the AA5083 materials. Fine filaments, oriented along the tensile axis, are observed on fracture surfaces and within surface cavities of specimens deformed primarily under grain-boundary-sliding creep. As deformation transitions to control by solute-drag creep, the density of these filaments dramatically decreases.

I. INTRODUCTION

COMMERCIAL aluminum alloy 5083 is the most commonly used material for superplastic forming (SPF) operations and is of particular importance to the transportation sector.[1,2] The recent commercial implementation of a proprietary version of SPF, designated "quick-plastic forming" (QPF), has brought SPF technology into large-scale, mass production for the automotive industry by lowering forming temperatures and shortening forming times compared to traditional SPF operations.[3] The deformation mechanism generally associated with superplasticity in fine-grained AA5083, such as commercially available superplastic-grade AA5083 materials, is grain-boundary-sliding (GBS) creep.[4–16] For the QPF process, however, temperatures are lower and strain rates are faster than in traditional SPF operations. It has been shown that the dominant deformation mechanism shifts toward solute-drag (SD) creep under these conditions,[12,17–19] as is observed in other commercial 5000-series alloys at elevated temperatures and slow strain rates.[20,21] The purpose of the present investigation is to examine the effects of this transition in deformation mechanisms on the tensile failure of commercial AA5083 materials.

Several investigators have studied the failure of AA5083 materials under conditions for which deformation is dominated by GBS creep. These include studies of failure under uniaxial tension[12,22–24] and under more complex loading situations.[25,26,27] These investigations reveal that failure is controlled by cavity nucleation, growth, and coalescence, leading finally to specimen rupture, when deformation is controlled by GBS creep under conditions typical of SPF operations. A variety of mechanisms have been proposed for cavity nucleation,[22,28,29] and a recent study supports the idea that cavities form preferentially under GBS creep in AA5083 at high-angle grain boundaries.[30] Cavitation damage limits the useful forming strains in SPF and QPF processes, even when there is no material rupture; cavity concentrations in excess of 2 vol pct typically degrade mechanical properties beyond acceptable performance requirements.[27] There is currently a lack of data on the failure of AA5083 materials deformed under conditions favorable for SD creep, which is a condition pertinent to QPF operations. For low-impurity Al-Mg materials deformed under SD creep, failure has been shown to be controlled by flow localization (*i.e.*, neck formation); in these low-impurity materials, final failure can occur by necking down to a sharp point.[31,32] For Al-Mg materials containing significant alloying or impurity additions, particularly those which tend to form intermetallic particles, and commercial 5000-series alloys, tensile deformation under SD creep is still controlled by flow localization.[20,33,34] However, final rupture in these materials occurs by cavity growth and coalescence in the reduced section of the neck.[20,33,34] Localized thinning during SPF or QPF processes can cause unacceptable geometric defects and lead to material rupture,[35,36] making an understanding of the conditions that favor this failure mechanism of direct technological importance. For the present investigation, mechanical testing was conducted on four AA5083 materials across temperatures and strain rates for which deformation is controlled by GBS creep, SD creep, and a combination of both deformation

MARY-ANNE KULAS, Graduate Student, is with the Materials Science and Engineering Program, The University of Texas at Austin, Austin, TX 78712-0292. W. PAUL GREEN, Engineer, is with Bell Helicopter Textron, Fort Worth, TX 76101. ERIC M. TALEFF, Associate Professor, is with the Materials Science and Engineering Program and the Department of Mechanical Engineering, The University of Texas at Austin. Contact e-mail: taleff@mail.utexas.edu PAUL E. KRAJEWSKI, Laboratory Group Manager, is with the Research and Development Center, General Motors Corp., Warren, MI 48090-9056. TERRY R. McNELLEY, Professor, is with the Department of Mechanical Engineering, Naval Postgraduate School, Monterey, CA 93943-5146.

Manuscript submitted March 2, 2005.

mechanisms. Failures of these materials are characterized as a function of deformation condition.

II. EXPERIMENTAL PROCEDURE

Four different AA5083 sheet materials were investigated in this study. The composition of each is given in Table I, along with sheet thickness and total true strain imposed by cold rolling during sheet production. All alloys have similar compositions, but each was produced using a different thermomechanical processing schedule. The materials labeled DC refer to sheet produced by hot and cold rolling from homogenized, direct-chill (DC) cast ingots, and the material labeled CC was cold rolled from a continuously cast (CC) slab. Previous investigations have revealed each of these AA5083 sheet materials to have fine recrystallized lineal-intercept grain sizes, ranging from 6.5 to 8.0 μm, which are resistant to static grain growth at temperatures of 500 °C and lower.[19] The recrystallized grain sizes of these materials, as previously reported,[19] are given in Table I with the standard deviations of the measurements.

Specimens used for mechanical testing had a "dog-bone" geometry with a gage length of either 25.4 or 50.8 mm. All specimens had a gage width of 6.0 mm and a gage thickness equal to that of the as-received sheet thickness (Table I). The shoulder radius of specimens was 7.9 mm. Specimens were tested in tension at elevated temperatures using rigid, shoulder-loading grips, which effectively restrict measurable plastic deformation to the gage region. The sheet rolling direction was always parallel to the tensile axis. Elongation-to-failure (EF) tests were performed at temperatures of 450 °C and 500 °C and strain rates from 3×10^{-4} to 6×10^{-2} s^{-1}. Temperature was controlled to within ±1 °C along each specimen gage length using a resistance furnace with three independent heating zones. Thermocouples were placed at each end of the gage length to ensure a uniform temperature. The EF tests used a "quasi-constant true strain rate," in which a constant true strain rate was simulated by a series of increasing constant crosshead speeds. Some elongation tests were stopped prior to failure so that cavitation behaviors could be studied at a specific local strain. Mechanical tests were conducted in a screw-driven, computer-controlled, electromechanical testing machine. Calipers were used to measure cross-sectional areas along specimens before and after testing.

Recrystallized sheet samples were mounted and polished for study of intermetallic particle distributions in each alloy by optical microscopy. Likewise, gage regions from tested EF samples were mounted and polished to measure cavity area fractions by optical microscopy. Images for particle analysis were digitally acquired at 200 times magnification for all DC materials, and images were acquired at 500 times for particle analysis of the CC material. The 200 times digital images for particle analysis were acquired at an image resolution of 0.50 μm/pixel. Particles 1.5 μm and larger were measured from these images, and all smaller objects were excluded from the analysis. The 500 times images for particle analysis in the CC material were acquired at a resolution of 0.20 μm/pixel. Particles 1.0 μm in diameter and larger were measured from these images. The particle cutoff sizes were taken from numerous calibration exercises used to determine the smallest particle sizes which could be consistently measured under repeated examination; the cutoff size varied with magnification and digital image resolution. All images used to measure cavity area fractions were taken at 200 times magnification. These images were acquired at resolutions of 0.50, 0.49, and 0.41 μm/pixel. Although microscopes with digital cameras of different resolutions were used, no differences in measurements between microscopes were found. Particle sizes and cavity area fractions were measured from digital images using three image-analysis software packages: CLEMEX VISION,* NIH ImageJ, and IMAGEPRO.** The calculated measurements were compared between the different software packages and were found to be independent of the software used. Particle sizes were measured as equivalent spherical diameters, and data from a minimum of four images were averaged for each material and condition. Cavity area fractions were also measured using several images for each calculation. Fracture surfaces and cavities developed at specimen surfaces during testing were studied using a JEOL† JSM-5610 scanning electron microscope (SEM) to acquire secondary-electron images.

*CLEMEX VISION is a trademark of Clemex Technologies, Inc., Longueuil, Canada.

**IMAGEPRO is a trademark of Media Cybernetics Inc., Silver Spring, MD.

†JEOL is a trademark of Japan Electronic Optics Ltd., Tokyo.

III. RESULTS AND DISCUSSION

A. *Tensile Ductilities and Failure Modes*

A previous investigation into the deformation mechanisms active during high-temperature deformation of the AA5083 materials listed in Table I revealed that all these materials deform in a very similar manner.[19] All deform by GBS creep at high temperatures and slow strain rates and by SD creep at low temperatures and fast strain rates. These behaviors

Table I. Sheet Thickness, t, Total Strain from Cold Rolling, ε_{cr}, Recrystallized Lineal-Intercept Grain Size, d, and Composition in Weight Percent of Each AA5083 Material

				Composition (Wt Pct)						
Material	t (mm)	ε_{cr}	d (μm)	Si	Fe	Cu	Mn	Mg	Cr	Al
DC-A	1.4	−1.3	6.9 ± 0.3	0.09	0.21	0.04	0.86	4.71	0.10	bal
DC-B	1.6	−1.3	6.6 ± 0.2	0.06	0.11	0.01	0.78	4.69	0.06	bal
DC-C	1.2	−1.3	6.5 ± 0.4	0.15	0.20	0.03	0.76	4.50	0.07	bal
CC-A	1.0	−1.6	8.0 ± 0.3	0.07	0.22	0.02	0.72	4.70	—	bal

are summarized in Figure 1, which contains plots of the logarithm of the Zener–Hollomon parameter, Z, against the logarithm of modulus-compensated stress, σ/E. Data are those for steady-state deformation taken from Reference 19. The SD creep was found to dominate deformation for $\sigma/E > 3 \times 10^{-4}$, while GBS creep dominates deformation for $\sigma/E < 3 \times 10^{-4}$. Figure 1 indicates this approximate division between mechanisms by dashed lines. In plotting Figure 1(a), the values of activation energy used to calculate Z are taken as those for the two dominant creep mechanisms, $Q_c = 110$ kJ/mole for GBS creep and $Q_c = 136$ kJ/mole for SD creep, with the transition between mechanisms occurring at approximately $\sigma/E = 3 \times 10^{-4}$.* Figure 1(a) makes clear that steady-state deformation is quite similar between the AA5083 materials, as all data fall onto the same curves. The use of two activation energies, however, causes a discontinuity in Z between the GBS and SD creep deformation regimes, as shown in Figure 1(a). Such a discontinuity makes the use of Z in describing deformation across both creep mechanisms awkward, at best. Fortunately, the similarity in activation energies between the two mechanisms makes it reasonable to use the convenient approximation of single Q_c values across both mechanisms. For plotting Figure 1(b), the activation energy across both creep mechanisms is approximated as $Q_c = 110$ kJ/mole, thus producing a single curve for data from all four AA5083 materials, to which a cubic polynomial fit is shown. A Q_c value equal to that for GBS deformation was chosen because of the importance of cavitation under this mechanism, which is discussed subsequently. A value of $Q_c = 110$ kJ/mole is used consistently throughout the remainder of the current study for calculation of Z values. Using this method of calculating Z, Figure 1(b) indicates a transition between deformation mechanisms at approximately $Z = 10^5$ s^{-1}.

*Please refer to Ref. 19 for a detailed discussion of activation energies throughout the GBS creep and SD creep deformation regimes.

Despite great similarities in deformation behaviors among the four AA5083 materials at small strains, as shown in Figure 1, these materials can produce remarkably different tensile ductilities. Tensile elongation is plotted as engineering strain to failure, e_f, against the logarithm of Z in Figure 2. The data in Figure 2 are clearly divided into two groups, which are indicated by the two trend lines fit to these data. The DC-A and DC-C materials exhibit large tensile ductilities, typically in excess of 300 pct, for $Z < 3 \times 10^5$ s^{-1}. The DC-B and CC-A materials, on the other hand, exhibit ductilities under 250 pct for the same deformation conditions. No indications of these tensile ductilities are given by the deformation data of Figure 1, which were taken at engineering strains of typically less than 35 pct. As Z increases above 3×10^5 s^{-1}, data from the high-ductility materials (DC-A and DC-C) and the low-ductility materials (DC-B and CC-A) nearly converge. However, the high-ductility materials continue to produce slightly larger elongations to failure at $Z > 3 \times 10^5$ s^{-1}. The Z value at which elongations of the high- and low-ductility materials diverge is very similar to that shown in Figure 1(b) as the transition between GBS and SD creep. This would indicate that tensile ductilities are similar among the different AA5083 materials when deformation is controlled by SD creep (high Z) and that

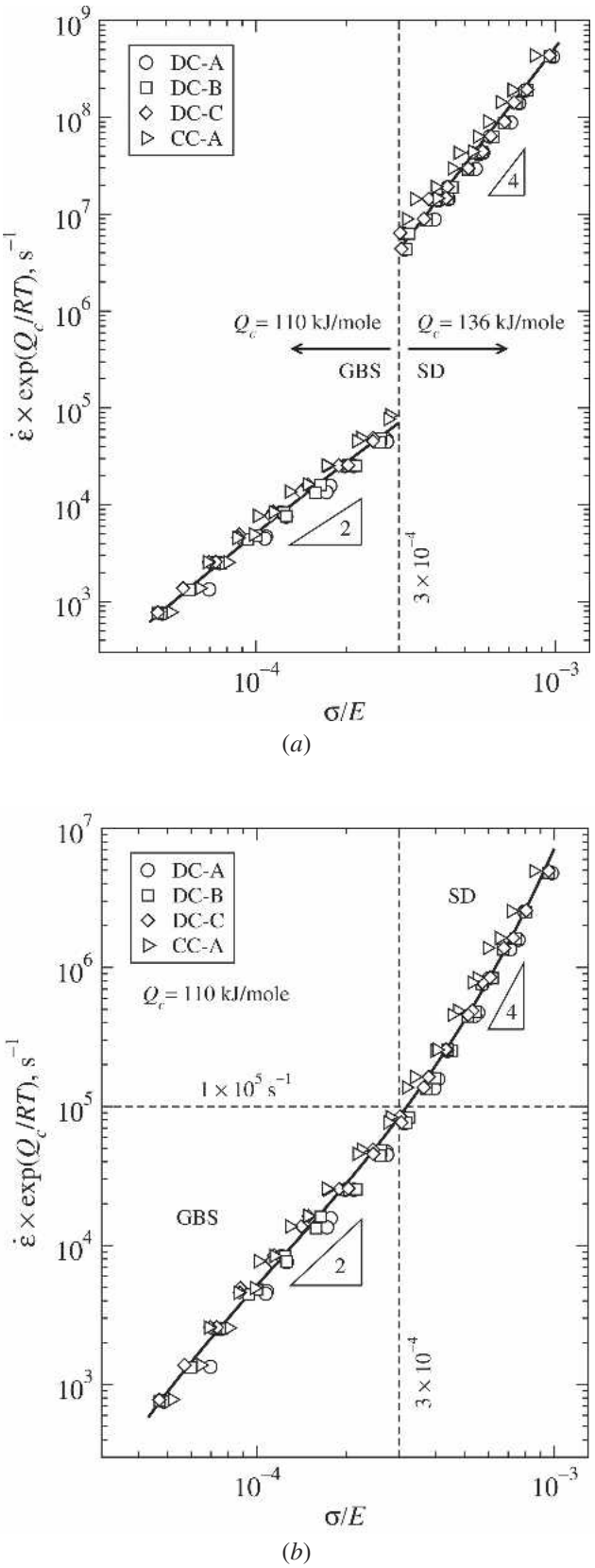

Fig. 1—The logarithm of the Zener–Hollomon parameter is plotted against the logarithm of modulus-compensated stress using (*a*) a unique value of activation energy for each deformation mechanism and (*b*) using a single value of $Q_c = 110$ kJ/mole across both deformation mechanisms. Data are from Reference 19.

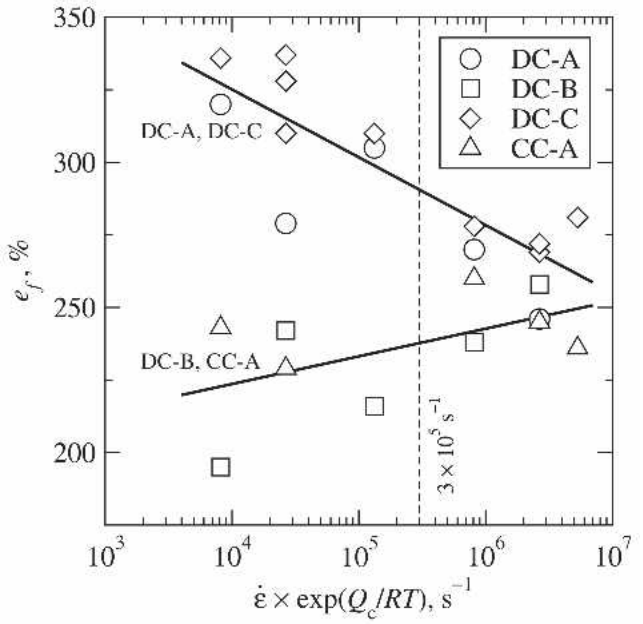

Fig. 2—Tensile elongations-to-failure, e_f, are plotted against the logarithm of the Zener–Hollomon parameter, calculated using a Q_c value of 110 kJ/mole.

deformation by GBS creep produces the large differences in ductility observed at low Z. Examination of failed specimens from the low-Z and high-Z conditions reveals a significant difference in the failure mechanisms. Figure 3(a) shows the failure region of a specimen tested at $Z = 5.3 \times 10^6$ s^{-1}, a condition for which SD creep controls deformation. This specimen failed after significant necking, both along its width and through its thickness. Final failure was by ductile fracture of the heavily necked region. In contrast to this behavior, Figure 3(b) shows a specimen tested at $Z = 2.6 \times 10^4$ s^{-1}, for which GBS creep controls deformation. This specimen failed by ductile fracture with no significant neck development. Furthermore, the surface of this specimen reveals many surface cavities characteristic of significant cavity coalescence. The consistent differences between the failures of specimens at high- and low-Z values indicate that two failure mechanisms are active: (1) cavitation and (2) flow localization (necking).

In order to quantify the degree of flow localization associated with final failures, reduction in area at the point of failure, q, was used to calculate a parameter designated here as Q.[17] The Q parameter is a comparison of the actual reduction in area to a theoretical reduction in area, q^*, without any flow localization. The theoretical reduction in area is calculated from elongation to failure, e_f, as

$$q^* = \left(1 - \frac{1}{1 + e_f}\right) \qquad [1]$$

The Q parameter can then be calculated as

$$Q = \frac{q - q^*}{q^*} \qquad [2]$$

and is represented for this investigation as a percent. A positive value of Q indicates flow localization. The greater the value of Q, the more macroscopic flow localization occurred

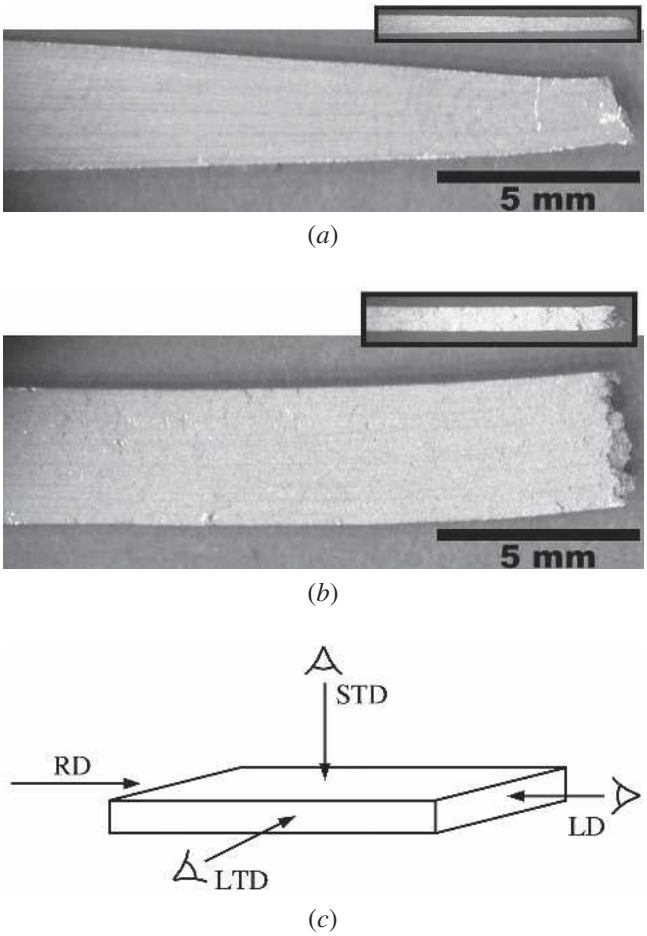

Fig. 3—The failure regions of DC-C specimens are shown for (*a*) failure controlled by necking when deformation is by SD creep ($T = 450$ °C, $\dot{\varepsilon} = 6 \times 10^{-2}$ s^{-1}) and (*b*) failure controlled by cavitation when deformation is by GBS creep ($T = 450$ °C, $\dot{\varepsilon} = 3 \times 10^{-4}$ s^{-1}). Primary views are in the STD orientation and inset views are in the LTD orientation, as shown in (*c*) the schematic, in which RD indicates rolling direction.

prior to failure, *i.e.*, the more severe is the neck formed. The presence of significant cavitation will decrease Q because volume will not be conserved during deformation. Thus, Q can attain negative values when there has been significant cavitation, particularly in the absence of flow localization. Calculated values of Q are plotted against the logarithm of the Zener–Hollomon parameter in Figure 4. For $Z > 3 \times 10^5$ s^{-1}, Q is positive, indicating that macroscopic flow localization plays an important part in specimen failures. At lower Z values, Q is negative, indicating that failure is controlled primarily by cavitation. The transition between failure controlled by flow localization and failure controlled by cavitation occurs at the same Z value denoted in Figure 2 for the divergence of ductility data. The Q values in Figure 4 and data in Figure 2 both indicate that flow localization controls failure under deformation by SD creep. Because the rate of flow localization depends on the strain rate sensitivity of the material,[37,38] and because all the AA5083 materials have similar strain-rate sensitivities when deformation is by SD creep (Figure 1), the ductilities of the AA5083 materials are all similar at high Z values. However, Figure 4 indicates that failure is controlled by cavitation when deformation is by GBS creep at low Z values, for which ductilities

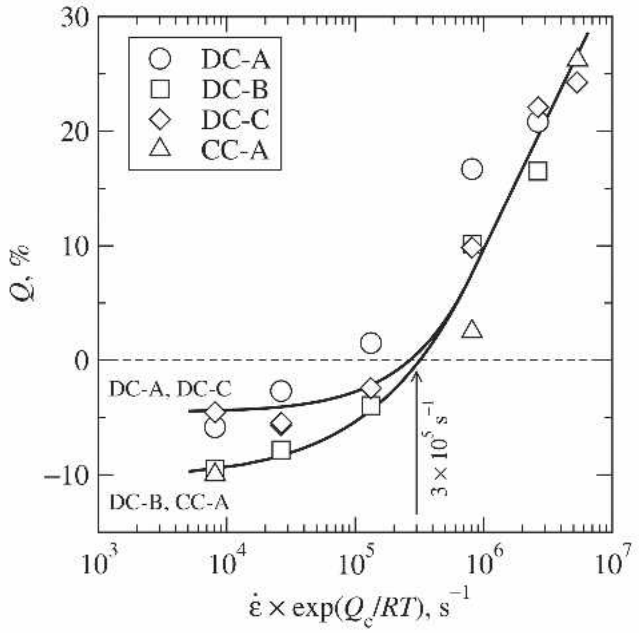

Fig. 4—Values of the Q parameter are plotted against the logarithm of the Zener–Hollomon parameter, Z, using a Q_c value of 110 kJ/mole. The Q parameter indicates that in all materials failure is dominated by necking when $Z > 3 \times 10^5\ s^{-1}$ and by cavitation when $Z < 3 \times 10^5\ s^{-1}$.

are quite different between the materials. This indicates that cavitation is likely more severe in materials DC-B and CC-A, which exhibit low ductilities, than in materials DC-A and DC-C. This is supported by the more negative Q values of materials DC-B and CC-A at low Z. Severe cavitation following neck formation in materials DC-B and CC-A may also explain the slightly earlier failure of these materials under conditions of SD creep, as early cavitation in the necked region would lead to a slightly earlier failure than in materials DC-A and DC-C. Furthermore, the decreasing elongations with decreasing Z of the DC-B and CC-A data in Figure 2 indicate that cavitation may be more severe in these materials under GBS creep than under SD creep.

B. *Cavitation and Intermetallic Particle Content*

In order to further investigate the suggestions of Figures 2 and 4 noted in Section A, the development of cavitation in each material was studied as a function of strain under conditions for which GBS creep controls deformation and under conditions for which SD creep controls deformation. The morphologies of cavitation developed under SD creep and under GBS creep are quite different, as is shown in Figure 5. Under SD creep (Figure 5(a)), cavities coalesce along the tensile axis into thin, stringerlike formations. Under GBS creep (Figure 5(b)), cavities coalesce in a more isotropic manner, with fewer stringerlike features and significant coalescence perpendicular to the tensile axis. Figure 5 indicates that the cavity morphology depends strongly on the mechanism governing deformation during cavity development. Cavity area fractions were measured from cross sections (LTD orientation) of tested specimens as a function of local reduction in area, from which local true strain was calculated. These data are plotted in Figure 6 as the logarithm of cavity area fraction *vs* true strain from local area reduction.

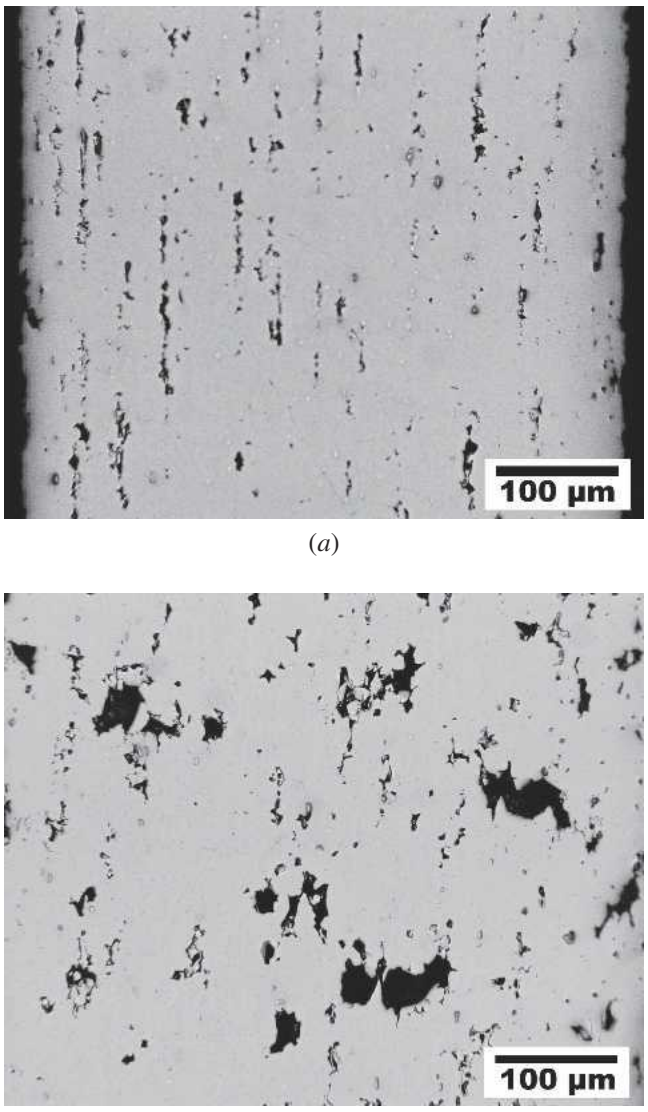

(*a*)

(*b*)

Fig. 5—Micrographs of material DC-C show cavity morphology under (*a*) SD creep ($T = 450$ °C, $\dot{\varepsilon} = 3 \times 10^{-2}\ s^{-1}$) and (*b*) GBS creep ($T = 450$ °C, $\dot{\varepsilon} = 3 \times 10^{-4}\ s^{-1}$) conditions. The tensile axis is vertical and the sheet thickness direction is horizontal in each image (LTD orientation). Micrographs are reproduced from Reference 18.

Data points shown in Figure 6 represent the average of several measurements using images from different locations in the specimen, and error bars represent the standard deviation of these measurements. Figure 6(a) presents data taken under conditions for which SD creep controls deformation, and Figure 6(b) presents data taken under conditions for which GBS creep controls deformation. Fits to the data sets in Figure 6 are shown using the following relationship:

$$V_f = V_0 \exp(\eta\varepsilon) \qquad [3]$$

where V_f is the volume fraction of cavities, which ideally equals the area fraction of cavities, ε is the true strain from area reduction, and V_0 and η are fitting parameters. The fitted parameters for each data set of Figure 6 are given in Table II. The good correlation of Eq. [3] with the data of Figure 6 is an indication that cavitation growth is likely plasticity controlled.[28,34] The term cavitation growth is used here to

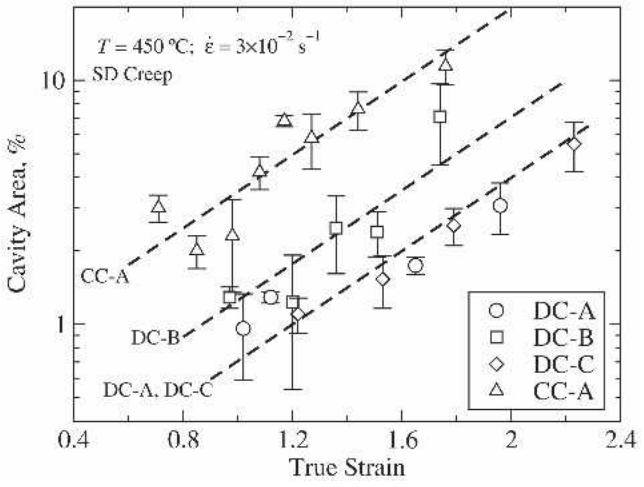

(*a*)

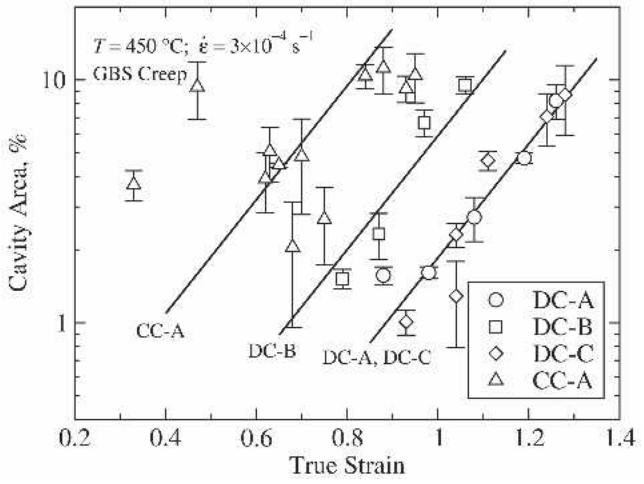

(*b*)

Fig. 6—The logarithm of measured cavity area fraction is plotted against true strain measured from reduction in area for (*a*) deformation under SD creep conditions ($T = 450$ °C, $\dot{\varepsilon} = 3 \times 10^{-2}\ s^{-1}$) and (*b*) deformation under GBS creep conditions ($T = 450$ °C, $\dot{\varepsilon} = 3 \times 10^{-4}\ s^{-1}$). The straight lines are fits to the data assuming a constant slope for each test condition.

Table II. Values of Parameters from Equation [3] Fit to the Data in Figure 6

	SD Creep		GBS Creep	
Material	V_0 (Pct)	η	V_0 (Pct)	η
DC-A, DC-C	0.13	1.7	0.0084	5.4
DC-B	0.22	1.7	0.027	5.4
CC-A	0.62	1.7	0.13	5.4

emphasize that it is the aggregate of cavity nucleation, growth, and coalescence that is being measured, as opposed to the growth of individual cavities, *i.e.*, a cavity growth rate.

To within the accuracy of data presented in Figure 6(a), the slopes of the data sets are approximately equal, and the data from materials DC-A and DC-C overlap. This indicates that the rate of cavitation growth with strain is the same for all three materials when deformation is by SD creep. An average value of $\eta = 1.7$ was used to enforce the observed constant slope for the fits shown in Figure 6(a); the corresponding values of V_0 for each material are given in Table II. Figure 6(a) indicates that the important difference in cavitation between the AA5083 materials, when deformed under SD creep, is the strain at which cavitation initially develops; the materials with the poorer tensile ductilities, CC-A and DC-B, develop significant cavitation at the earliest strains. Once significant cavitation is developed, however, cavitation growth occurs at approximately the same rate with plastic straining, regardless of the material. Data for cavitation growth when deformation is by GBS creep, shown in Figure 6(b), reveal similar trends. To within the data scatter, which is quite significant for the CC-A material, all the data sets in Figure 6(b) exhibit a similar slope, with data from materials DC-A and DC-C again overlapping. The fits shown in Figure 6(b) enforce a constant slope for all the materials by using an average value of $\eta = 5.4$; the corresponding values of V_0 for each material are given in Table II. Again, the materials with poorer tensile ductilities develop significant cavitation at the earliest strains. Once significant cavitation has developed, the rate of cavitation growth with strain is similar between the materials when deformation is by GBS creep. The early cavitation in materials DC-B and CC-A explains both their low ductilities and their more negative values of Q when failure is controlled by cavitation, *i.e.*, deformation is by GBS creep. The significant scatter in data from the continuously cast CC-A material, which does not occur for deformation under SD creep, is notable; the reasons for this large scatter are not currently known. The fits from Figure 6 are reproduced in Figure 7 for comparison of behaviors between deformation by SD creep and by GBS creep. Also indicated in Figure 7 is the approximate maximum cavity content acceptable for commercial SPF processes.[27] From Figure 7, it is clear that the cavitation growth rate with strain is significantly faster when deformation is by GBS creep than when deformation is by SD creep.

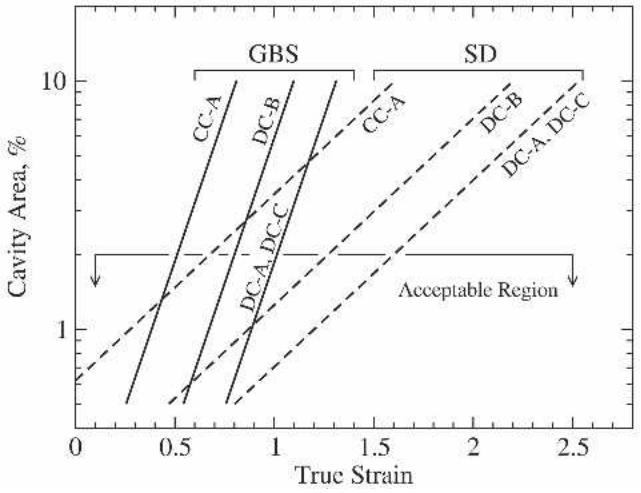

Fig. 7—Fitted curves from Figure 6 are reproduced for comparison between behaviors under SD creep conditions and under GBS creep conditions.

Evidence has been cited for the association of cavitation in superplastic AA5083 materials with the presence of intermetallic particles,[15,18,22–24] particularly with $(Mn,Fe)Al_6$ and $(Fe,Mn)Si_2Al_{15}$ intermetallic products,[39] which are necessary for the development of fine, stable grain sizes. Typical examples of intermetallic particles are shown in the optical micrographs of Figure 8 for (a) a DC cast material, DC-C, and (b)

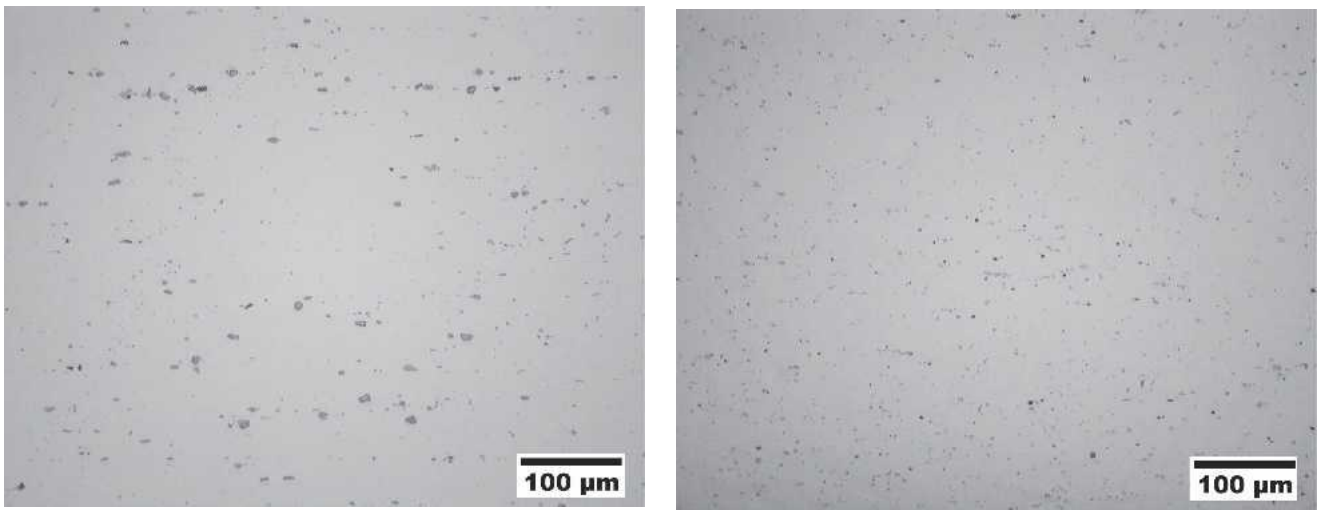

(*a*) (*b*)

Fig. 8—Micrographs of materials (*a*) DC-C and (*b*) CC-A show examples of intermetallic particles, presumably dominated by $(Mn,Fe)Al_6$ and $(Fe,Mn)Si_2Al_{15}$.[39] The particles in the CC material are visibly finer than those of the DC material. Views are in the STD orientation, and the rolling direction is horizontal.

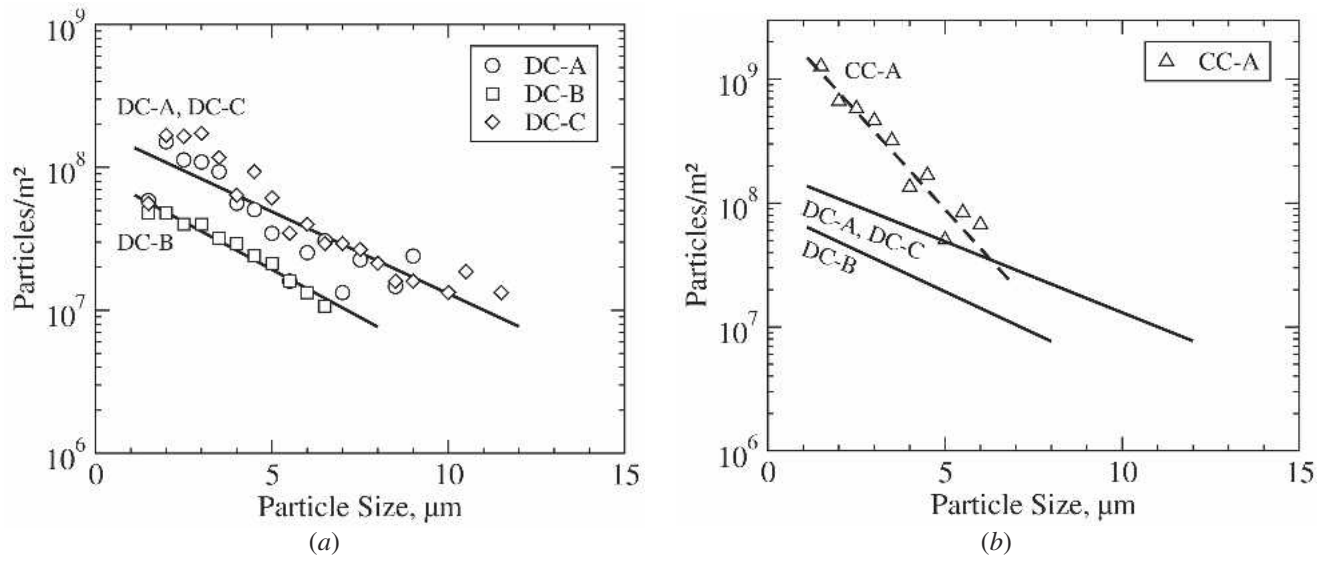

(*a*) (*b*)

Fig. 9—The logarithm of particle area density is plotted against particle size for (*a*) the DC materials and (*b*) material CC-A. The curves shown are from fits to the data, and the curves for the DC materials are repeated in (*b*) for comparison.

CC material, CC-A. The intermetallic particles in the CC material are finer than those in the DC cast materials. Data for intermetallic particle-size population density are shown in Figure 9, in which only particle-size bins containing a minimum of five counts are displayed. Particle-size population densities are shown in Figure 9(a) for the DC cast materials. The distributions of particles in the DC-A and DC-C materials overlap, and a single curve is fit to both these data sets. The population of particles in the DC-B material reside below that of the DC-A and DC-C materials. As seen in Table I, all the alloys contain approximately the same amounts of intermetallic-forming elements. It is, therefore, reasonable to expect that all the DC cast materials would have nearly the same total volume fraction of intermetallic particles. If this is the case, then it could be concluded from Figure 9(a) that material DC-B might contain a number of large intermetallic particles, which are not within the detectable range of the measurement technique. The measurement technique attempts to ensure statistical significance of the data by truncating the range of measurements to exclude data from particles at sizes for which only a few particles are measured. Thus, data from scarce large particles are unlikely to be considered, even if a few happened to be observed in the 2-D metallographic sections. Even a small number of large particles could be the cause of the early development of cavitation in material DC-B. Figure 9(b) presents the fits from Figure 9(a) with data from the CC-A material. These data indicate that material CC-A has a significantly larger number of fine intermetallic particles than do the DC cast materials, as was qualitatively observed in Figure 8. The early cavitation of material CC-A under SD creep is consistent with a previous investigation of DC cast and CC AA5182 materials, in which it was observed that the CC material exhibited significantly earlier cavitation than did the DC cast material.[20] The early cavitation of the

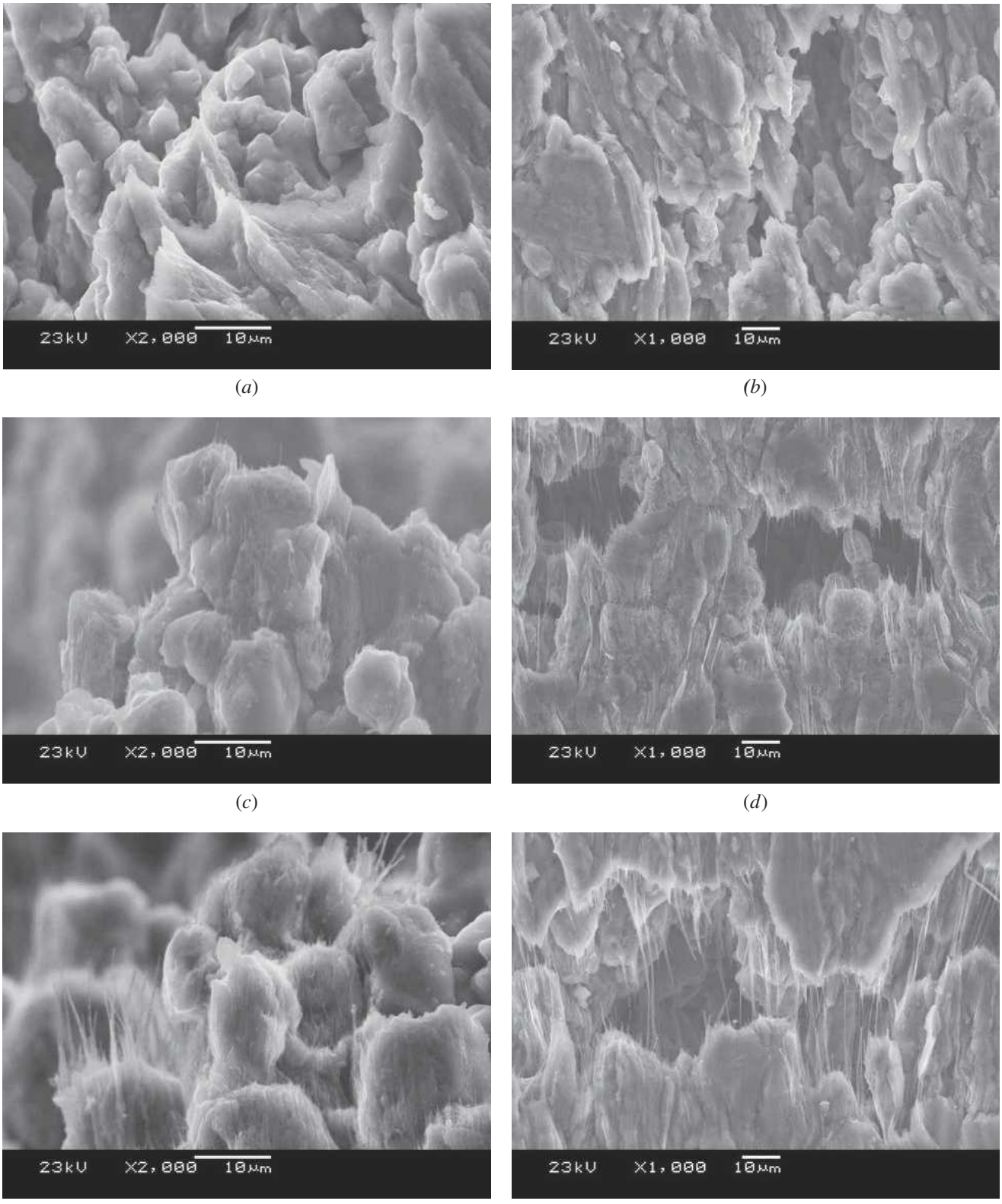

Fig. 10—A series of micrographs for material DC-C is shown illustrating the transition from SD creep to GBS creep. The left column shows fracture surfaces under (*a*) SD creep, (*c*) transition from GBS to SD creep, and (*e*) GBS conditions. The right column shows surface cavity openings under (*b*) SD creep, (*d*) transition from GBS to SD creep, and (*f*) GBS conditions. The tensile axis is approximately vertical in all images.

CC-A material under GBS creep, for which cavitation develops at smaller strains than in any of the DC cast materials, does not fit the explanation proposed previously for early cavitation of the DC-B material. It must be concluded that understanding the cavitation behavior of the CC-A material, in comparison to the DC cast materials, requires additional data.

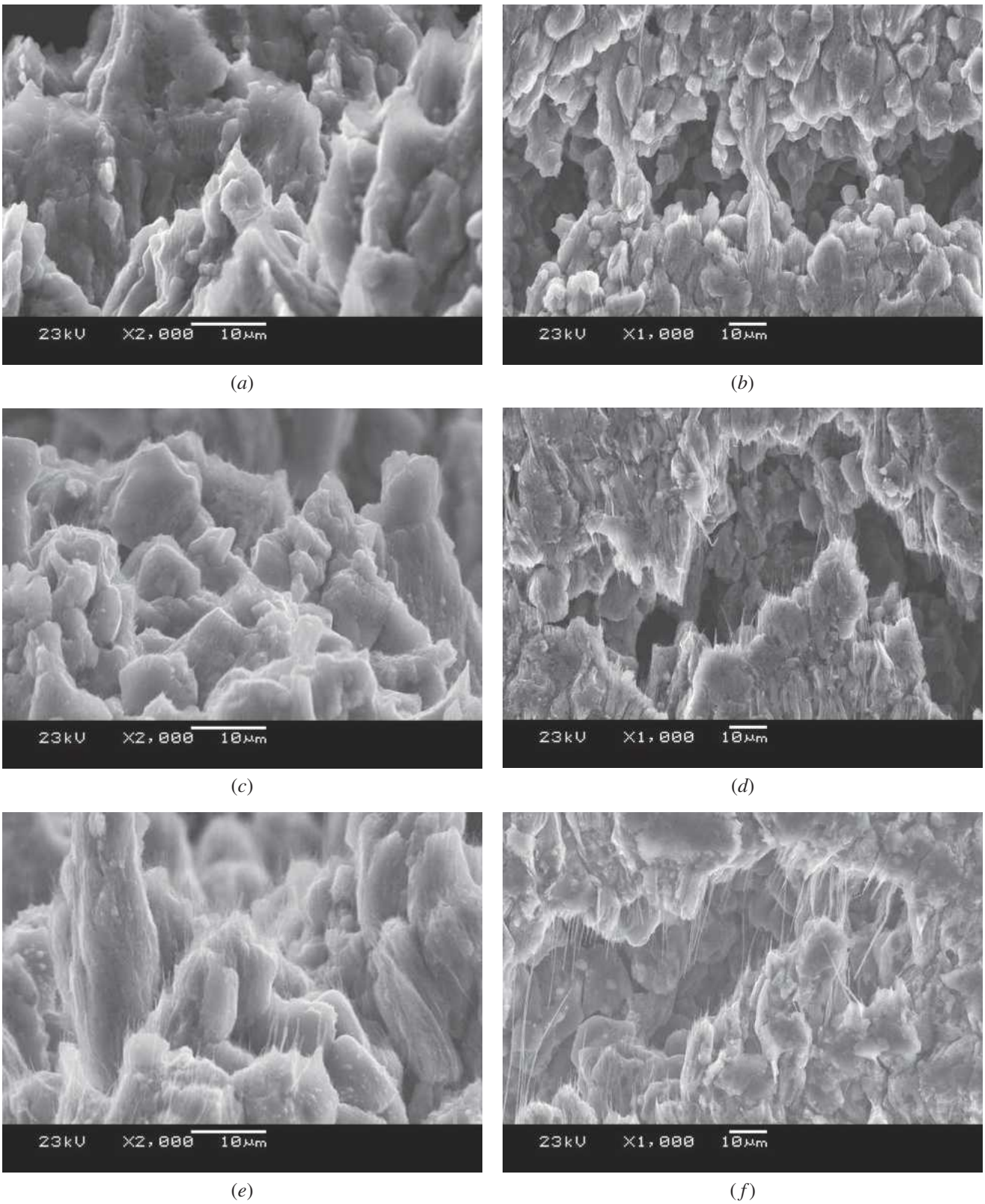

Fig. 11—A series of micrographs for material CC-A is shown illustrating the transition from SD creep to GBS creep. The left column shows fracture surfaces under (*a*) SD creep, (*c*) transition from GBS to SD creep, and (*d*) GBS conditions. The right column shows surface cavity openings under (*b*) SD creep, (*d*) transition from GBS to SD creep, and (*f*) GBS conditions. The tensile axis is approximately vertical in all images.

C. *Fracture Surface Morphologies*

Fracture surfaces and cavities opened on specimen surfaces near failure regions were examined in a SEM to characterize differences in failure morphologies between conditions for which deformation is by SD creep and conditions for which deformation is by GBS creep. Fracture surfaces and surface

cavities were observed from specimens of materials DC-C and CC-A tested under three different conditions: (1) $\dot{\varepsilon} = 3 \times 10^{-2}\ s^{-1}$ at $T = 500\ °C$ ($Z = 8.1 \times 10^5\ s^{-1}$), for which deformation is controlled by SD creep, (2) $\dot{\varepsilon} = 3 \times 10^{-4}\ s^{-1}$ at $T = 450\ °C$ ($Z = 2.7 \times 10^4\ s^{-1}$), for which deformation is on the GBS side of the transition to SD creep, and (3) $\dot{\varepsilon} = 3 \times 10^{-4}\ s^{-1}$ at $T = 500\ °C$ ($Z = 8.1 \times 10^3\ s^{-1}$), for which deformation is fully controlled by GBS creep. The SEM micrographs of the fracture surfaces and surface cavities from the DC-C material for these testing conditions are shown in Figure 10, and SEM micrographs from the CC-A material for identical testing conditions are shown in Figure 11. These micrographs exhibit the following features. Fracture surfaces and surface cavities formed under SD creep exhibit the characteristics of ductile fracture with large local plasticity and deformation structures elongated in the tensile direction. Fracture surfaces and surface cavities formed under GBS creep exhibit the characteristics of ductile failure at grain boundaries, and a large density of submicrometer fibers are evident on the fracture surfaces. These fibers protrude from the fracture surface along the tensile direction and bridge surface cavities along the direction of tensile deformation. Fibers are not evident on fracture surfaces or in surface cavities formed under SD creep. Fracture surfaces formed under conditions near the transition from GBS to SD creep exhibit a mixture of the features described previously, with some fibers protruding from fracture surfaces and within surface cavities, but at a significantly lower density than those observed for the GBS creep condition. These failure morphologies provide further clear evidence of a transition in failure mechanism, which roughly corresponds with the previously described transition in deformation mechanism.

Similar submicrometer fibers have been previously observed on the fracture surfaces of superplastically deformed AA5083[12] and AA7475,[40,41] as well as for aluminum-matrix composites.[42] A variety of explanations have been proposed for the origins of these submicrometer fibers.[42] Figures 10 and 11, however, provide clear evidence from which at least two important conclusions can be drawn. First, fiber formation is distinctly associated with deformation by GBS creep. As a result, fiber formation is likely to be specifically associated with local grain boundary plasticity. Second, fiber formation cannot be the result of incipient melting or the formation of a glassy phase at grain boundaries. Figures 10 and 11 clearly show that at a single temperature, 500 °C for the given micrographs, fiber formation can be induced by simply reducing the imposed strain rate. Furthermore, fibers are not produced at 500 °C when deformation is by SD creep but are formed at the lower temperature of 450 °C when strain rate is reduced sufficiently to produce significant GBS creep deformation. These results are not consistent with incipient melting nor with glassy phases at grain boundaries as explanations for fiber formation.

IV. CONCLUSIONS

Mechanisms of tensile failure at elevated temperatures have been evaluated in four AA5083 materials. Two mechanisms control final failure: cavitation and flow localization (necking). Failure occurs by cavitation when deformation is controlled by GBS creep. Failure occurs by flow localization when deformation is controlled by SD creep. Even when flow localization controls failure, final failure is by cavity coalescence in the heavily necked region. The Q parameter, which is calculated from local reduction in area at failure and specimen elongation to failure, serves as a quantitative means of evaluating the relative importance of flow localization *vs* cavitation for failed specimens. Two of the AA5083 materials, DC-A and DC-C, provide high tensile ductilities, which increase with the decreasing Zener–Hollomon parameter, Z. The remaining two AA5083 materials, DC-B and CC-A, produce slightly lower ductilities at high Z, but their ductilities decrease with decreasing Z, thus producing poor tensile ductilities under conditions typical of SPF operations. The differences between these materials are related to cavitation behaviors. Cavities produced when deformation is by SD creep have morphologies different from those produced when deformation is by GBS creep. Furthermore, the cavitation growth rate under SD creep is significantly slower than that under GBS creep. All four AA5083 materials exhibit a similar cavitation growth rate under a given deformation mechanism. However, those materials with poor ductility exhibit significant cavitation at much earlier strains than do those with good ductility. These differences in strains at which significant cavitation first develops correlate with intermetallic particle size populations. For DC cast materials, a reduction in the number of large intermetallic particles, which should produce an increase in the number of fine intermetallic particles for a constant alloy composition, may improve ductility. However, for the CC material, which has large populations of fine particles, additional factors, which require further investigation, appear to encourage cavitation and produce poor ductility. Finally, the development of submicrometer fibers on fracture surfaces and within surface cavities was shown to be specifically associated with deformation by GBS creep.

ACKNOWLEDGMENT

The authors gratefully acknowledge support from the General Motors Corp. for this work.

REFERENCES

1. K. Osada and K. Shirkawa: in *Advances in Superplasticity and Superplastic Forming*, E.M. Taleff, P.A. Friedman, P.E. Krajewski, R.S. Mishra, and J.G. Schroth, eds., TMS, Warrendale, PA, 2004, pp. 41-49.
2. http://www.superform-aluminium.com/.
3. J.G. Schroth: in *Advances in Superplasticity and Superplastic Forming*, E.M. Taleff, P.A. Friedman, P.E. Krajewski, R.S. Mishra, and J.G. Schroth, eds., TMS, Warrendale, PA, 2004, pp. 9-20.
4. A. Ball and M.M. Hutchison: *Met. Sci. J*., 1969, vol. 3, pp. 1-7.
5. O.D. Sherby and J. Wadsworth: in *Superplasticity in Aerospace*, H.C. Heikkenen and T.R. McNelley, eds., TMS, Warrendale, PA, 1988, pp. 3-27.
6. H. Fukuyo, H.C. Tsai, T. Oyama, and O.D. Sherby: *Iron Steel Inst. Jpn. Int*., 1991, vol. 31, pp. 76-85.
7. T.G. Langdon: *Mater. Sci. Eng*., 1991, vol. A137, pp. 1-11.
8. J.S. Vetrano, C.A. Lavender, C.H. Hamilton, M.T. Smith, and S.M. Bruemmer: *Scripta Metall*., 1994, vol. 30, pp. 565-70.
9. R. Verma, P. Friedman, A. Ghosh, C. Kim, and S. Kim: *J. Mater. Eng. Performance*, 1995, vol. 4, pp. 543-50.
10. R. Verma, P. Friedman, A. Ghosh, S. Kim, and C. Kim: *Metall. Mater. Trans. A*, 1996, vol. 27A, pp. 1889-98.
11. T.G. Nieh, J. Wadsworth, and O.D. Sherby: *Superplasticity in Metals and Ceramics*, Cambridge University Press, Cambridge, United Kingdom, 1997, pp. 40-53.

12. Y. Takayama, S. Sasaki, T. Tozawa, H. Kato, H. Watanabe, and M. Kokubo: *J. Jpn. Inst. Light Met*., 1999, vol. 49, pp. 378-82.
13. D.H. Bae and A.K. Ghosh: *Acta Mater*., 2000, vol. 48, pp. 1207-24.
14. I.C. Hsiao and J.C. Huang: *Metall. Mater. Trans. A*, 2002, vol. 33A, pp. 1373-84.
15. R.M. Cleveland, A.K. Ghosh, and J.R. Bradley: *Metall. Mater. Trans. A*, 2003, vol. 351, pp. 228-36.
16. P.A. Friedman and W.B. Copple: in *Hot Deformation of Aluminum Alloys III*, Z. Jin, A. Beaudoin, T.A. Bieler, and B. Radhakrishnan, eds., TMS, Warrendale, PA, 2003, pp. 211-19.
17. M.-A. Kulas, P.E. Krajewski, T.R. McNelley, and E.M. Taleff: in *Hot Deformation of Aluminum Alloys III*, Z. Jin, A. Beaudoin, T. Bieler, and B. Radhakrishnan), eds., TMS, Warrendale, PA, 2003, pp. 499-507.
18. M.-A. Kulas, W.P. Green, E.C. Pettengill, P.E. Krajewski, and E.M. Taleff: in *Advances in Superplasticity and Superplastic Forming*, E.M. Taleff, P.A. Friedman, P.E. Krajewski, R.S. Mishra, and J.G. Schroth, eds., TMS, Warrendale, PA, 2004, pp. 127-38.
19. M.-A. Kulas, W.P. Green, E.M. Taleff, P.E. Krajewski, and T.R. McNelley: *Metall. Mater. Trans. A*, 2005, vol. 36A, pp. 1249-61.
20. E.M. Taleff, P.J. Nevland, and P.E. Krajewski: *Metall. Mater. Trans. A*, 2001, vol. 32A, pp. 1119-30.
21. E.M. Taleff: *Advances in Superplasticity and Superplastic Forming*, E.M. Taleff, P.A. Friedman, P.E. Krajewski, R.S. Mishra, and J.G. Schroth, eds., TMS, Warrendale, PA, 2004, pp. 85-94.
22. D.H. Bae and A.K. Ghosh: *Acta Mater*., 2002, vol. 50, pp. 511-23.
23. D.H. Bae and A.K. Ghosh: *Acta Mater*., 2002, vol. 50, pp. 993-1009.
24. D.H. Bae and A.K. Ghosh: *Acta Mater*., 2002, vol. 50, pp. 1011-29.
25. D.H. Bae, A.K. Ghosh, and J.R. Bradley: *Metall. Mater. Trans. A*, 2003, vol. 34, pp. 2449-63.
26. J.R. Bradley: in *Advances in Superplasticity and Superplastic Forming*, E.M. Taleff, P.A. Friedman, P.E. Krajewski, R.S. Mishra, and J.G. Schroth, eds., TMS, Warrendale, PA, 2004, pp. 109-18.
27. J.R. Bradley and J.E. Carsley: in *Advances in Superplasticity and Superplastic Forming*, E.M. Taleff, P.A. Friedman, P.E. Krajewski, R.S. Mishra, and J.G. Schroth, eds., TMS, Warrendale, PA, 2004, pp. 149-57.
28. M.A. Khaleel, H.M. Zbib, and E.A. Nyberg: *Int. J. Plast*., 2001, vol. 17, pp. 277-96.
29. D.H. Bae and A.K. Ghosh: *Mater. Sci. Eng. A*, 2002, vol. A322, pp. 233-40.
30. K. Oh-ishi, J.F. Boydon, and T.R. McNelley: in *Advances in Superplasticity and Superplastic Forming*, E.M. Taleff, P.A. Friedman, P.E. Krajewski, R.S. Mishra, and J.G. Schroth, eds., TMS, Warrendale, PA, 2004, pp. 119-26.
31. E.M. Taleff, D.R. Lesuer, and J. Wadsworth: *Metall. Mater. Trans. A*, 1996, vol. 27A, pp. 343-52.
32. E.M. Taleff, W.-J. Kim, and O.D. Sherby: in *Modeling the Mechanical Response of Structural Materials*, E.M. Taleff and R.K. Mahidhara, TMS, Warrendale, PA, 1998, pp. 209-18.
33. E.M. Taleff and P.J. Nevland: *JOM*, 1999, vol. 51, pp. 34-36.
34. E.M. Taleff, T. Leon-Salamanca, R.A. Ketcham, R. Reyes, and W.D. Carlson: *J. Mater. Res*., 2000, vol. 15, pp. 76-84.
35. N.R. Harrison, S.G. Luckey, P.A. Friedman, and Z.C. Xia: in *Advances in Superplasticity and Superplastic Forming*, E.M. Taleff, P.A. Friedman, P.E. Krajewski, R.S. Mishra, and J.G. Schroth, eds., TMS, Warrendale, PA, 2004, pp. 301-09.
36. K. Murali, G.P. Montgomery, Jr., and J.G. Schroth: in *Advances in Superplasticity and Superplastic Forming*, E.M. Taleff, P.A. Friedman, P.E. Krajewski, R.S. Mishra, and J.G. Schroth, TMS, Warrendale, PA, 2004, pp. 311-21.
37. M.A. Burke and W.D. Nix: *Acta Metall*., 1975, vol. 23, pp. 793-98.
38. J.W. Hutchinson and H. Obrecht: *Fracture*, 1977, vol. 1, pp. 101-16.
39. S. Kim, M.P. Balogh, and R.A. Waldo: in *Advances in Superplasticity and Superplastic Forming*, E.M. Taleff, P.A. Friedman, P.E. Krajewski, R.S. Mishra, and J.G. Schroth, eds., TMS, Warrendale, PA, 2004, pp. 139-48.
40. J.J. Blandin, B. Hong, A. Varloteaux, M. Suery, and G. L'Esperance: *Acta Mater*., 1996, vol. 44, pp. 2317-26.
41. W.D. Cao, X.P. Lu, and H. Conrad: *Acta Mater*., 1996, vol. 44, pp. 697-706.
42. M.G. Zelin: *Acta Mater*., 1997, vol. 45, pp. 3533-42.